

Experimental determination of the Ag L -subshell x-ray-production cross sections by electron impact through two bulk target methods

Tabatha P. Rodríguez and Andrés H. Sepúlveda 

Facultad de Ciencias Naturales, Matemática y del Medio Ambiente, Universidad Tecnológica Metropolitana (UTEM), 7800002 Santiago, Chile

Pablo D. Pérez 

Centro Científico Tecnológico Patagonia Norte, CONICET, Centro Atómico Bariloche, 8402 San Carlos de Bariloche, Argentina

Jorge C. Trincavelli and Gustavo Castellano *

Instituto de Física Enrique Gaviola (IFEG-CONICET), Facultad de Matemática, Astronomía, Física y Computación (FaMAF), Universidad Nacional de Córdoba, 5000 Córdoba, Argentina



(Received 23 August 2022; revised 2 December 2022; accepted 25 January 2023; published 9 February 2023)

The experimental determination of x-ray-production cross sections by electron impact on thick samples is faced in this work, especially focusing on the L subshells of Ag. The integrodifferential method used by An *et al.* is compared with a recently implemented approach involving the ionization distribution function. The first method has shown good results under suitable conditions, namely, when multiple scattering, bremsstrahlung enhancement, and other secondary effects are negligible. Monte Carlo simulations were performed in order to analyze the influence of these conditions and therefore to extend the validity range of the method by adding a correction factor. The second approach uses the ionization distribution function $\phi(\rho z)$ to predict the intensity of the emitted photons; this magnitude is assessed by the POEMA software, previously developed, and it is used to determine correction factors to the cross sections included in the software database. Both approaches were tested by fitting several L -shell spectra measured in a wide interval of incident electron energies, ranging from 4.0 to 25 keV, with an electron microprobe equipped with a wavelength-dispersive spectrometer. The x-ray-production cross sections obtained for each L subshell and the total L x-ray-production cross section were compared with theoretical predictions based on the distorted-wave approach theory and with experimental determinations when available.

DOI: [10.1103/PhysRevA.107.022806](https://doi.org/10.1103/PhysRevA.107.022806)

I. INTRODUCTION

The adequate knowledge of ionization cross sections by electron impact is crucial in the understanding of the interaction of electrons with atoms and also of the subsequent relaxation of the ionized atom. Ionization cross sections are among the essential atomic magnitudes needed in a wide range of applications in different areas of applied science and technology, particularly in several techniques for materials characterization.

Several theoretical models have been developed for the calculation of ionization cross sections, such as the plane-wave Born approximation (PWBA) [1–4], the distorted-wave approach (DWBA) [5–8] and the binary-encounter Bethe model [9–11]. Although to a first approximation positron and electron cross sections can be considered identical, the electrostatic repulsion from the nucleus makes positrons less effective; in addition, the indistinguishability of electron projectiles introduces the so-called exchange scattering [8]. Experimental determinations are always necessary for a reliable validation of these theoretical models; however,

L -subshell measured data are rather scarce in the literature for most elements, mainly due to the difficulties inherent to the experiment, such as the deconvolution of multiple peaks and knowledge of the detector efficiency. This latter becomes relevant because the analysis of L spectra usually covers an energy range where the efficiency varies considerably.

Separate L -subshell ionization cross sections for Ag in the low energy range of 4–25 keV have rarely been surveyed through experiments; for some of these energies, total L -shell x-ray-production cross-section values have been reported [12], whereas ionization cross-section data have been given for higher energies [13–15].

Different alternatives may be chosen to experimentally determine x-ray-production cross sections with keV electrons. In this work two methods using bulk pure targets were explored to determine silver cross sections, which were compared with other results previously obtained through a thin sample approach. Along the present work, experimental values have been obtained on one hand by means of an integrodifferential method [16,17], which assumes the electrons describe linear trajectories within the irradiated material, maintaining their incident direction; in addition, some improvements were introduced through Monte Carlo simulations with the purpose of correcting for losses due to the assumptions made. On the

*gcas@famaf.unc.edu.ar

TABLE I. Incident electron energy E_o , current, and total cumulative time per channel (totaling 1200 channels per spectrum).

E_o (keV)	Current (nA)	Time per channel (s)	E_o (keV)	Current (nA)	Time per channel (s)
4.0	19.98	33.6	13	35.02	2.5
4.2	19.98	33.6	14	30.03	2.5
4.4	19.99	33.6	15	50.12	1.4
4.6	20.00	33.6	16	50.05	1.4
4.8	20.01	33.6	17	20.02	1.4
5.0	20.04	33.6	18	19.99	3.0
6.0	50.07	9.0	19	20.00	3.0
6.5	60.04	7.2	20	20.00	3.0
7.0	69.97	3.0	21	19.99	3.0
8.0	70.06	2.8	22	19.98	3.0
9.0	69.60	2.5	23	17.98	3.0
10.0	49.80	2.5	24	17.01	3.0
11.0	50.00	2.5	25	15.99	3.0
12.0	40.01	2.5	—	—	—

other hand, an approach is proposed involving the ionization distribution function $\phi(\rho z)$, which has been implemented in the code POEMA, developed in previous works [18,19]. Both methods were tested in a set of L -shell spectra corresponding to electron beam energies ranging from 4.0 to 25 keV and compared with other data, when available.

II. EXPERIMENTAL

A. Material and measurements

The spectra were acquired in a commercial JEOL 8230 electron microprobe. A bulk pure Ag standard was irradiated with electrons at normal incidence ($\alpha = 0^\circ$). The spectra were

recorded by means of a wavelength-dispersive spectrometer (WDS) equipped with a curved PET crystal ($2d = 8.742 \text{ \AA}$) configured in Johansson geometry and a sealed P10 Xe proportional counter aligned with a take-off angle of 40° . The acquisition time and electron current were modified for each incident energy to achieve acceptable statistical uncertainties while minimizing sample damage as much as possible, since these damages might cause systematic errors on the emitted photon intensities. With this idea in mind, the specimen was irradiated in an accumulative routine for each incident energy, scanning the target surface with the electron probe over a preset grid scheme; in this way, no specimen regions were irradiated for extended periods of time. The electron incident energies E_o , beam currents, and total acquisition times used are listed in Table I. As an example, Fig. 1 displays a measured spectrum corresponding to a 10-keV electron beam.

In order to guarantee sample conductivity (and also to avoid irradiation damages), a carbon layer was sputtered by the manufacturer onto the standard set surface, since each of the standards included is embedded in an insulator resin. The measured thickness of this layer was $(63 \pm 1) \text{ nm}$, as determined in a previous work [20]. This material thickness modifies the electron incident energy profile reaching the Ag target, and its influence on the cross sections assessed is analyzed in detail in Sec. III.

B. Efficiency of the wavelength-dispersive spectrometer

The absolute efficiency of a WDS at the photon energy E_k can be defined as

$$\varepsilon(E_k) = \frac{N_k/n_o}{T_k},$$

where N_k is the measured intensity area for the x-ray characteristic line k , n_o is the number of incident electrons, and

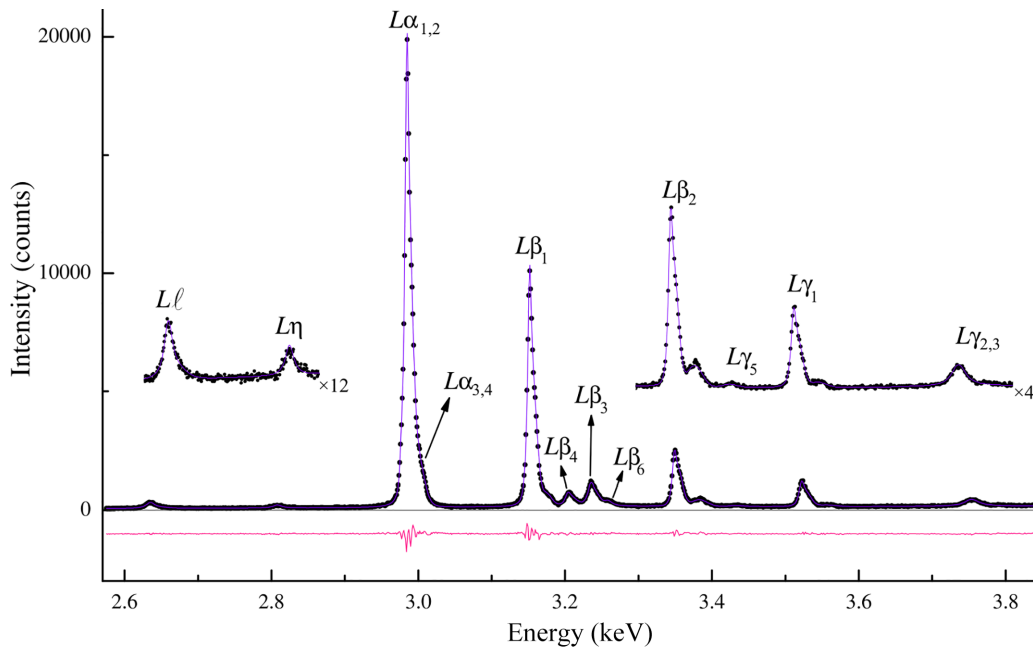


FIG. 1. L -shell x-ray spectrum emitted by a thick Ag target bombarded with 10-keV electrons. The inset graphs are magnifications with the same horizontal scale. • Experimental; — spectrum fitting; — fitting residues.

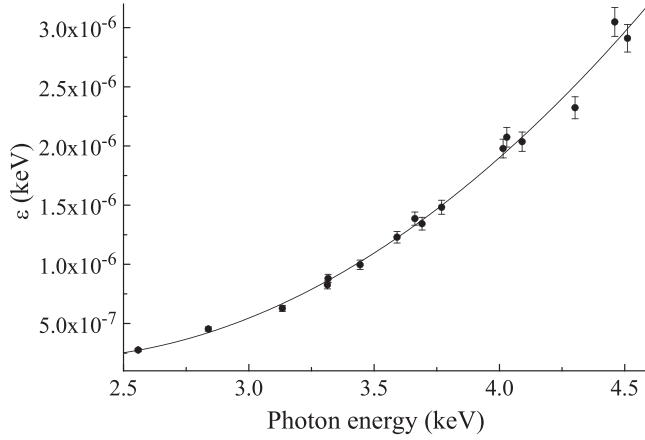


FIG. 2. Absolute efficiency of the spectrometer WDS-PET. • Experimental values; — fitting curve.

T_k is the number of Ag characteristic photons emitted per incident particle. According to this definition, the efficiency bears energy units [21].

With the aim of determining this efficiency, the value T_k must be known in a wide range of emitted photon energies. This value does not depend on the spectrometer used, nor on the measuring time, and therefore T_k was determined by acquiring several spectra using an energy-dispersive spectrometer (EDS) attached to the microprobe, at an incident energy of 15 keV. This N₂-cooled 10-mm² active area Si(Li) detector is sealed by a 77% open area Formvar window 166-nm thickness, supported by a silicon grid of 380 μm depth. In this case the number of measured characteristic photons I_{EDS} is related to T_k through

$$T_k = \frac{1}{n} \sum_i \frac{I_{\text{EDS}}(E_i)}{\frac{\Delta\Omega}{4\pi} \varepsilon'(E_i)}, \quad (1)$$

where $\Delta\Omega$ is the solid angle subtended by the detector window from the electron impact point on the target surface, $\varepsilon'(E_i)$ is the EDS intrinsic efficiency at the photon energy E_i (as an example, $\varepsilon'(3 \text{ keV}) = 0.7486$), n is the number of incident electrons in the EDS measurement, and the summation covers all the channels i embraced in the characteristic peak. The complete procedure to determine the intrinsic efficiency was detailed in [22], and the solid angle used in this work was $(1.15 \pm 0.05) \times 10^{-4} \text{ sr}$ [21].

The results obtained for ε are shown in Fig. 2, along with the quadratic fitting obtained. It is worth noting that this efficiency curve covers almost entirely the full working energy range of the PET crystal. To achieve this efficiency curve, K spectra from K, Ca, Sc, Ti, V, Cr, and Mn pure targets, and L spectra from Ru, Pd, Cd, Sn, and Te pure targets were used.

C. Carbon coating

The surface carbon coating degrades the monoenergetic electron distribution entering the Ag target. With the purpose of providing the electron energy distribution emerging from the carbon coating and impinging on the Ag target, Monte Carlo simulations were carried out with the main program PENCYL. Electron beams impinging an isolated carbon layer

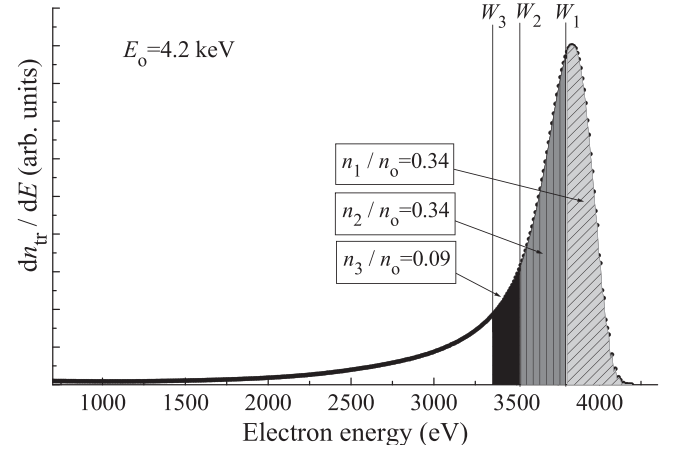


FIG. 3. Energy distribution for 4.2-keV electrons after traversing the carbon layer. The vertical lines show the binding energies W_i for each shell L_i . The ratio of the number of electrons in each category relative to the total number of electrons is shown in boxes.

of 63 nm, the coating thickness on top of the analyzed target, were simulated for the incident energies listed in Table I. As an example, Fig. 3 displays the energy distribution obtained for 4.2-keV electrons, where the broadening of the electron energy distribution is clearly evidenced. It can also be seen that although the beam energy is greater than all L -shell binding energies W_i , after traversing the carbon coating a fraction of electrons may bear energies unable to ionize every subshell. For each E_o , the resulting energy distribution dn_{tr}/dE for the electrons emerging the carbon layer towards the Ag target—i.e., the number of electrons transmitted across the carbon coating with energies in the interval $[E, E + dE]$ — can be grouped into four categories, as compared to each of the three L -subshell energy levels; the total number of incident electrons n_o can therefore be expressed as

$$n_o = n_- + n_3 + n_2 + n_1, \quad (2)$$

where n_- is the number of electrons which cannot ionize any L subshell; n_3 labels those electrons reaching the Ag target with energies between the W_3 and W_2 ; n_2 , between W_2 and W_1 , and n_1 , above the W_1 level. These n_i values and the average energies E_i associated to each electron group are obtained as

$$n_i = \int_{W_i}^{W_{i-1}} \frac{dn_{\text{tr}}}{dE} dE, \quad (3)$$

$$E_i = \frac{1}{n_i} \int_{W_i}^{W_{i-1}} E \frac{dn_{\text{tr}}}{dE} dE,$$

where $W_o \equiv E_o$.

It is useful to define the total proportion of electrons that bear sufficient energy to ionize each shell,

$$F_i = \frac{1}{n_o} \sum_{j \leq i} n_j, \quad (4)$$

and their respective effective energy

$$E_{L_i}^{\text{ef}} = \frac{\sum_{j \leq i} n_j E_j}{\sum_{j \leq i} n_j}. \quad (5)$$

TABLE II. Energy and fraction of effective electrons for each L subshell, associated with each incident energy.

E_o (keV)	$E_{L_1}^{ef}$ (keV)	$E_{L_2}^{ef}$ (keV)	$E_{L_3}^{ef}$ (keV)	F_1	F_2	F_3
4.0	–	3.65(4)	3.59(5)	–	0.434	0.631
4.2	3.90(2)	3.79(5)	3.75(5)	0.342	0.683	0.769
4.4	4.03(3)	3.96(6)	3.94(6)	0.652	0.797	0.844
4.6	4.19(5)	4.15(6)	4.13(7)	0.784	0.860	0.889
4.8	4.38(6)	4.34(7)	4.32(7)	0.854	0.901	0.920
5.0	4.57(6)	4.54(7)	4.52(7)	0.896	0.927	0.940
6.0	5.57(8)	5.56(7)	5.56(7)	0.970	0.974	0.976
6.5	6.09(8)	6.09(7)	6.08(7)	0.978	0.980	0.981
7.0	6.61(7)	6.61(6)	6.61(6)	0.982	0.983	0.984
8.0	7.65(7)	7.65(6)	7.65(6)	0.986	0.987	0.987
9.0	8.68(7)	8.68(5)	8.68(5)	0.988	0.989	0.989
10.0	9.70(6)	9.70(5)	9.70(5)	0.990	0.990	0.990
11.0	10.73(6)	10.72(7)	10.72(7)	0.991	0.991	0.991
12.0	11.74(8)	11.74(7)	11.74(7)	0.992	0.992	0.992
13.0	12.76(7)	12.75(7)	12.75(7)	0.992	0.993	0.993
14.0	13.77(7)	13.77(7)	13.77(7)	0.993	0.993	0.993
15.0	14.78(7)	14.78(7)	14.78(7)	0.993	0.993	0.994
16.0	15.79(7)	15.79(7)	15.79(7)	0.994	0.994	0.994
17.0	16.80(7)	16.79(7)	16.79(7)	0.994	0.994	0.994
18.0	17.80(7)	17.80(7)	17.80(7)	0.994	0.994	0.995
19.0	18.81(7)	18.81(7)	18.81(7)	0.995	0.995	0.995
20.0	19.82(7)	19.81(7)	19.81(7)	0.995	0.995	0.995
21.0	20.82(7)	20.8(1)	20.8(1)	0.995	0.995	0.995
22.0	21.8(1)	21.8(1)	21.8(1)	0.996	0.996	0.996
23.0	22.8(1)	22.8(1)	22.8(1)	0.996	0.996	0.996
24.0	23.8(1)	23.8(1)	23.8(1)	0.996	0.996	0.996
25.0	24.8(1)	24.8(1)	24.8(1)	0.996	0.996	0.996

The values obtained for F_i and $E_{L_i}^{ef}$ are displayed in Table II, where it can be seen that the effect produced by the carbon layer becomes more relevant for beam energies below 6 keV, since in these cases a non-negligible percentage of the incident electrons bear energy which cannot ionize all three L subshells.

III. METHODS FOR CROSS-SECTION DETERMINATION

Special care must be taken in the analysis of multiple atomic shell ionizations, since primary vacancies can be rearranged through Coster-Kronig transitions [23]. This process modifies the emission of the characteristic x-rays and thus it is convenient to define the final vacancy ionization cross sections $\tilde{\sigma}_{L_i}$ associated with the L_i level, from the primary ionization cross sections σ_{L_i} :

$$\begin{aligned}\tilde{\sigma}_{L_1} &= \sigma_{L_1} \\ \tilde{\sigma}_{L_2} &= \sigma_{L_2} + f_{12} \sigma_{L_1} \\ \tilde{\sigma}_{L_3} &= \sigma_{L_3} + f_{23} \sigma_{L_2} + (f_{13} + f_{12}f_{23}) \sigma_{L_1}.\end{aligned}\quad (6)$$

From these expressions, the x-ray-production cross section $\sigma_{L_i}^x$ can be obtained for each subshell by using the corresponding fluorescence yield ω_{L_i} ,

$$\sigma_{L_i}^x = \omega_{L_i} \tilde{\sigma}_{L_i}.\quad (7)$$

This definition allows a connection of predicted cross sections with experimental data. The different alternatives chosen for performing these comparisons are detailed below.

A. Modified integrodifferential method

This approach is based on the differentiation of an analytical expression for the number of detected characteristic photons P_k with respect to E_o . There are two main assumptions in the original model [16]: (1) the incident electron follows a rectilinear trajectory within the target, and (2) the radiation generated from secondary particles is negligible. For n_o incident electrons, the number of detected photons for a certain decay k to a vacancy in the L_i subshell can then be expressed as

$$\begin{aligned}P_k(E_o) &= n_o \frac{N_A}{A} f_k \omega_{L_i} \varepsilon \int_0^R d(\rho z) \tilde{\sigma}_{L_i}(E(\rho z)) \\ &\times \exp \left[-\mu(E_k) \frac{\cos \alpha}{\sin \theta_t} \int_0^{\rho z} d(\rho z') \right],\end{aligned}\quad (8)$$

where N_A is the Avogadro's number, A is the Ag atomic mass, f_k is the relative transition probability of the characteristic line k , ρz is the sample mass depth, $\mu(E_k)$ is the mass attenuation coefficient at the corresponding k characteristic line energy, θ_t is the take-off angle, R is the range of the electrons with energy capable of ionizing the atomic shell of interest, and α is the angle of incidence measured from the target surface normal.

Recalling the electron stopping power definition [24] $S(E) = -dE/d(\rho z)$, Eq. (8) can be rewritten as

$$\begin{aligned}P_k(E_o) &= n_o \frac{N_A}{A} f_k \omega_{L_i} \varepsilon \int_{W_i}^{E_o} \frac{dE}{S(E)} \tilde{\sigma}_{L_i}(E) \\ &\times \exp \left[-\mu(E_k) \frac{\cos \alpha}{\sin \theta_t} \int_E^{E_o} \frac{dE'}{S(E')} \right],\end{aligned}\quad (9)$$

where W_i is the binding energy of the L_i subshell. This expression can be differentiated with respect to E_o using Leibniz's rule to take into account that the differentiation variable is present in the integral limits as well as in the integrand, which leads to

$$\begin{aligned}\tilde{\sigma}_{L_i}(E_o) &= \frac{A}{n_o N_A} \frac{1}{f_k \omega_{L_i} \varepsilon} \\ &\times \left[S(E_o) \frac{d}{dE_o} (P_k(E_o)) + P_k(E_o) \mu(E_k) \frac{\cos \alpha}{\sin \theta_t} \right].\end{aligned}\quad (10)$$

In order to obtain $\tilde{\sigma}_{L_i}$ through this approach, both P_k and its derivative must be known, and a numerical differentiation of the experimental data may be necessary [16]. However, in the present work a suitable function optimally representing the data curve for $T_k(E_o) = P_k(E_o)/(n_o \varepsilon)$ was found as detailed below, whose analytical derivative can be readily assessed.

With the aim of extending the range of applicability for this approach, the experimental T_k values were corrected by means of a function G for the intensity changes due to photons generated after ionization by secondary particles, and also for the straggling of electrons, which sets them apart from their rectilinear trajectories. The latter effect increments the

amount of ionizations and subsequent x-ray emission, particularly originating in shallow layers from which characteristic photons are less attenuated, whereas backscattering losses produce a decrease in the registered intensities.

The correction function G was assessed from the ratio between the number of photons per incident particle P_{cal} associated to a given subshell L_i , capable of reaching the detector, as calculated from Eq. (8), and the corresponding magnitude obtained through Monte Carlo simulations P_{sim} . These estimates were obtained by means of the main program PENCYL, included in the PENELOPE code [25], taking into account all the transitions available in its database. On the other hand, with the aim of calculating P_{cal} , values for the electron stopping power, cross sections, absorption coefficients, and fluorescence yields were also taken from the PENELOPE database. The simulations were run until an average of 4% relative uncertainty was achieved for the intensities of the L_3 characteristic lines, which yielded an average of 7% relative uncertainty for the L_2 group and a 22% for the L_1 group.

The values obtained for each L_i group were respectively fitted with analytical functions \bar{P}_{cal} and \bar{P}_{sim} , similar to Eq. (11) given below, which were finally used to provide the correction function $G = \bar{P}_{\text{cal}}/\bar{P}_{\text{sim}}$. From the definition for the WDS efficiency, Eq. (10) is better expressed as a function of the photon intensity emitted by the target per incident electron $T_k(E_o) = P_k(E_o)/(n_o \varepsilon)$, for which the fitting function chosen here is

$$\exp[c_1(E_o - c_2)^{-c_3}](c_4 E_o^{-c_5} - c_6), \quad (11)$$

where the parameters c_i were determined through an optimization algorithm.

To determine the subshell cross sections separately, all the peak intensities associated to the same subshell were grouped, after converting to emitted photons by dividing the integrand by ε ,

$$\bar{T}_k(E_o) = \frac{G}{F_i} T_k = \frac{G}{F_i n_o} \int_{E_k-w}^{E_k+w} \frac{I(E)}{\varepsilon(E)} dE,$$

where w is an energy value such that the interval between $E_k - w$ and $E_k + w$ embraces all the photons emitted by the transition involved, and $(G/F_i)T_k$ is the new normalized peak intensity.

The sums $T_{L_i}(E_{L_i}^{\text{ef}})$ of all these corrected intensities associated to the transitions to the subshell L_i for each incident energy $E_{L_i}^{\text{ef}}$, were fitted with a function analogous to Eq. (11). Figure 4 displays the values obtained for T_{L_i} , as well as the uncorrected values (with $G = 1$), in order to evidence the influence of the G factor. As can be seen, if the corrections introduced here are neglected, important overestimations result for all subshells, which are reflected in the assessment of the corresponding x-ray-production cross sections, as shown below.

Taking into account all these definitions, the x-ray-production cross section can be restated as

$$\sigma_{L_i}^x(E_{L_i}^{\text{ef}}) = \frac{A}{N_A} \times \sum_k \left[S(E_{L_i}^{\text{ef}}) \frac{d\bar{T}_k(E_{L_i}^{\text{ef}})}{dE_{L_i}^{\text{ef}}} + \bar{T}_k(E_{L_i}^{\text{ef}}) \mu(E_k) \frac{\cos \alpha}{\sin \theta_t} \right]. \quad (12)$$

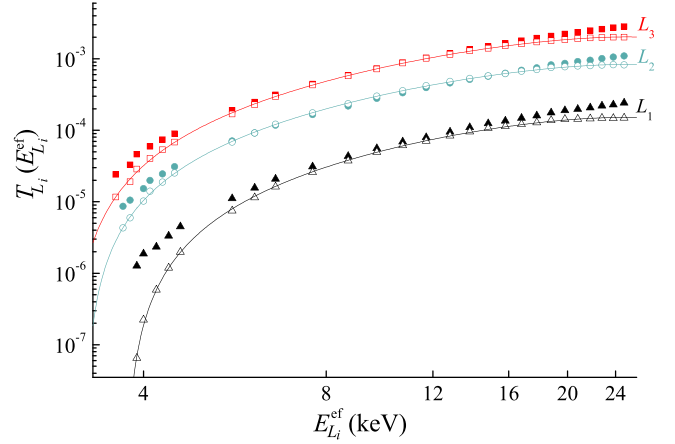


FIG. 4. Total generated photon number per incident particle $T_{L_i}(E_o)$ for each L_i subshell, along with the corresponding summation of the fitting curves $\bar{T}_k(E_o)$ [see Eq. (11)]. Solid symbols: integrodifferential method ($G = 1$); empty symbols: modified integrodifferential method.

B. Ionization distribution approach

In this second approach, the ionization cross sections were obtained by means of the POEMA software [18], designed for processing experimental spectra in electron probe microanalysis. This software is based on the optimization of a set of parameters associated with an analytical function that describes the experimental spectrum; the ionization cross section is one of those parameters. The spectral fitting is achieved by minimizing the normalized quadratic differences between the experimental intensities I_i and the analytical function \bar{I}_i used to predict the spectrum,

$$\chi^2 = \frac{1}{N_c - N_p} \sum_{i=1}^{N_c} \frac{(\bar{I}_i - I_i)^2}{I_i},$$

where N_c is the number of channels, and N_p is the number of parameters to be refined. The uncertainties related to the parameters obtained are estimated by propagating the errors of the experimental channel intensities by numerical differentiation [26]. To perform this assessment, all the models involved in the analytical description of the spectrum (\bar{I}_i) are assumed to bear negligible uncertainties; this approximation is reasonable, since the main contributions to the resulting uncertainties are due to experimental statistical errors, which are more relevant in the case of weak lines.

For a pure target with atomic number Z , the analytical expression for the intensity \bar{I}_i with photon energy E_i (within an energy interval ΔE) in the i th channel is

$$\bar{I}_i = B(Z, E_o, E_i) + \sum_k P_k H_k(E_i), \quad (13)$$

where $B(Z, E_o, E_i)$ is the background radiation, and P_k and H_k are respectively the intensity and peak profile for a given transition k . This latter term is proportional to the final vacancy ionization cross section $\tilde{\sigma}_{L_i}$ and also involves the detector efficiency $\varepsilon(E_k)$, as well as other atomic and experimental parameters [27].

TABLE III. X-ray production cross sections (in barn) determined in this work. Columns labeled A: modified integrodifferential method; columns labeled B: ionization distribution function approach.

E_o (keV)	σ_L^x		$E_{L_1}^{\text{ef}}$ (keV)	$\sigma_{L_1}^x$		$E_{L_2}^{\text{ef}}$ (keV)	$\sigma_{L_2}^x$		$E_{L_3}^{\text{ef}}$ (keV)	$\sigma_{L_3}^x$	
	A	B		A	B		A	B		A	B
4.0	–	–	–	–	–	3.65(4)	67(14)	–	3.59(5)	165(42)	–
4.2	380(110)	410(92)	3.90(2)	4(2)	7(2)	3.79(5)	77(14)	42(10)	3.75(5)	206(65)	107(23)
4.4	420(140)	469(80)	4.03(3)	6(3)	15(3)	3.96(6)	93(20)	82(15)	3.94(6)	224(82)	205(33)
4.6	450(100)	514(69)	4.19(5)	9(5)	17(3)	4.15(6)	101(29)	102(15)	4.13(7)	254(51)	263(34)
4.8	470(49)	549(68)	4.38(6)	13(4)	21(2)	4.34(7)	113(17)	121(16)	4.32(7)	280(20)	311(38)
5.0	490(48)	577(59)	4.57(6)	15(5)	23(2)	4.54(7)	123(14)	131(13)	4.52(7)	301(23)	340(36)
6.0	560(57)	655(45)	5.57(8)	24(6)	32(2)	5.56(7)	154(17)	175(12)	5.56(7)	369(33)	424(29)
6.5	580(61)	673(40)	6.09(8)	26(6)	35(2)	6.09(7)	161(17)	179(10)	6.08(7)	386(37)	443(27)
7.0	600(64)	683(36)	6.61(7)	28(6)	37(2)	6.61(6)	170(17)	190(10)	6.61(6)	399(39)	453(24)
8.0	610(54)	688(32)	7.65(7)	30(5)	39(2)	7.65(6)	170(16)	188(9)	7.65(6)	411(31)	460(21)
9.0	620(51)	682(30)	8.68(7)	31(6)	41(2)	8.68(5)	169(16)	188(8)	8.68(5)	413(29)	458(20)
10.0	630(52)	672(29)	9.70(6)	31(6)	41(2)	9.70(5)	169(16)	189(8)	9.70(5)	412(30)	449(20)
11.0	620(53)	658(31)	10.73(6)	32(6)	42(2)	10.72(7)	168(16)	184(8)	10.72(7)	414(31)	441(21)
12.0	620(52)	643(30)	11.74(8)	31(6)	40(2)	11.74(7)	167(16)	183(8)	11.74(7)	412(30)	433(21)
13.0	610(47)	626(26)	12.76(7)	31(5)	40(2)	12.75(7)	165(14)	176(7)	12.75(7)	406(27)	413(17)
14.0	600(47)	610(25)	13.77(7)	31(5)	40(2)	13.77(7)	163(15)	171(7)	13.77(7)	407(27)	405(17)
15.0	590(47)	593(24)	14.78(7)	31(5)	39(2)	14.78(7)	160(15)	165(7)	14.78(7)	400(27)	390(16)
16.0	580(47)	577(24)	15.79(7)	30(5)	38(2)	15.79(7)	158(14)	160(7)	15.79(7)	398(28)	380(16)
17.0	570(46)	561(24)	16.80(7)	29(5)	37(2)	16.79(7)	156(14)	156(7)	16.79(7)	392(27)	366(15)
18.0	560(47)	545(23)	17.80(7)	29(5)	36(1)	17.80(7)	153(15)	152(6)	17.80(7)	388(28)	359(15)
19.0	550(45)	530(22)	18.81(7)	29(5)	36(1)	18.81(7)	152(14)	151(6)	18.81(7)	382(28)	347(15)
20.0	540(48)	515(22)	19.82(7)	28(5)	35(1)	19.81(7)	147(15)	144(6)	19.81(7)	374(29)	338(14)
21.0	520(52)	500(21)	20.82(7)	26(6)	33(1)	20.8(1)	144(18)	140(6)	20.8(1)	365(29)	328(14)
22.0	510(48)	486(21)	21.8(1)	25(5)	33(1)	21.8(1)	138(15)	135(6)	21.8(1)	355(28)	319(14)
23.0	500(45)	472(20)	22.8(1)	24(5)	32(1)	22.8(1)	134(13)	132(6)	22.8(1)	344(27)	311(14)
24.0	490(45)	459(20)	23.8(1)	23(4)	31(1)	23.8(1)	129(14)	129(5)	23.8(1)	333(27)	304(13)
25.0	480(41)	446(19)	24.8(1)	22(4)	31(1)	24.8(1)	123(12)	126(5)	24.8(1)	318(24)	295(13)

To consider the effect of the carbon coating, the total number of detected photons in the k line, corresponding to a decay to an L_j vacancy, accumulates the separate contribution $P_k^{n_i}$ of each electron group n_i ,

$$P_k = \sum_{i \geq j} P_k^{n_i}, \quad (14)$$

taking into account the corresponding average energy E_i for each group. For example, in the case of a line k corresponding to a decay to the L_3 subshell and generated by the i th electron group,

$$P_k^{n_i} = n_i f_k \omega_{L_3} \tilde{\sigma}_{L_3}(E_i) \varepsilon(E_k) (ZAF)_k. \quad (15)$$

The ionization depth-distribution function $\phi(\rho z)$ is determinant in the ZAF matrix corrections [28]. It is clear that the specific ability of each electron group to ionize a particular subshell is characterized by the average energies E_i , in this case furnishing three final vacancy ionization cross sections:

$$\begin{aligned} \tilde{\sigma}_{L_3}(E_3) &= \sigma_{L_3}(E_3) \\ \tilde{\sigma}_{L_3}(E_2) &= \sigma_{L_3}(E_2) + f_{23} \sigma_{L_2}(E_2) \\ \tilde{\sigma}_{L_3}(E_1) &= \sigma_{L_3}(E_1) + f_{23} \sigma_{L_2}(E_1) + (f_{13} + f_{12} f_{23}) \sigma_{L_1}(E_1). \end{aligned} \quad (16)$$

If the cross sections are approximated by a linear function $\sigma_{L_i}(E) = a_i E + b_i$ (a_i, b_i constants) in the energy interval

$[E_1, E_3]$, P_k can be written in a compact fashion in terms of the corresponding effective energies (5):

$$P_k \approx n_o f_k \omega_{L_3} \varepsilon(E_k) (ZAF)_k \left[\sigma_{L_3}(E_{L_3}^{\text{ef}}) F_3 + f_{23} \sigma_{L_2}(E_{L_2}^{\text{ef}}) F_2 + (f_{13} + f_{12} f_{23}) F_1 \sigma_{L_1}(E_{L_1}^{\text{ef}}) \right]. \quad (17)$$

By means of the optimization procedure, this equation is used to relate the experimental intensity P_k with the searched values of the ionization cross sections $\sigma_{L_1}(E_{L_1}^{\text{ef}})$, $\sigma_{L_2}(E_{L_2}^{\text{ef}})$, and $\sigma_{L_3}(E_{L_3}^{\text{ef}})$. A similar analysis can be done for the lines corresponding to decays to the L_2 and L_1 subshells, leading to additional expressions which complement Eq. (17). The resulting equations are particularly relevant for low beam energies, when the number of electrons with energy enough to ionize each subshell can be significantly reduced after traversing the carbon coating, leading to the possibility that ionizations in certain subshell may become unattainable.

Regarding the strategy followed during the fitting of the Ag spectra with the software POEMA, parameters like relative transition probabilities and natural linewidths were also optimized, bearing in mind the high resolution of the spectrometer used. Taking into account the characteristic energies obtained in a previous work [29], all the observed peaks were fitted with Voigt profiles, achieving a very good agreement between experimental and predicted spectra ($\chi^2 < 2$ in every case), as can be seen in Fig. 1.

TABLE IV. Fluorescence yields coefficients and Coster-Kronig transition probabilities used in this work: a, Perkins *et al.* [35]; b, Campbell [36].

	Fluorescence yields			Coster-Kronig probabilities		
	ω_1	ω_2	ω_3	f_{12}	f_{13}	f_{23}
a	0.014879	0.054703	0.057018	0.09211	0.6644	0.1604
b	0.016	0.051	0.052	0.068	0.57	0.141

IV. RESULTS AND DISCUSSION

A. Modified integrodifferential method

Table III displays the values obtained for $\sigma_{L_i}^x$ corresponding to each subshell, in which the data for the electron stopping power S and the x-ray attenuation coefficient were extracted from the PENELOPE database [25]. The uncertainties were obtained by error propagation on Eq. (12), assigning an uncertainty of 5% to the stopping power, according to [30], and 5% to the x-ray attenuation coefficients [31]. The uncertainty for the derivatives for the fitting functions at a given energy was estimated from the difference between the average of two numerical derivatives of contiguous measured data and the analytical derivative of Eq. (11). Furthermore, the uncertainties associated to the solid angle (4%), the beam current ($\sim 0.2\%$), and G were added quadratically, these latter being estimated by error propagation of the statistical uncertainties for the simulated P_{sim} (see Sec. III A). No relevant statistical uncertainties were introduced in the estimate of the values for F_n . On the other hand, the uncertainty associated to each effective energy $E_{L_i}^{\text{ef}}$ was assessed as three times the standard deviation of the weighted average energy from each simulated energy distribution for the electrons transmitted through the carbon coating.

B. Ionization distribution function approach

Table III also displays the results obtained for $\sigma_{L_i}^x$ using the ionization distribution function approach. The uncertainties were determined from relative error propagation of the beam current ($\sim 0.2\%$), the peak intensities obtained from numerical differentiation ($\sim 1.5\%$), and the detector efficiency (4%). Additionally, the effects produced by the variation on the effective energies were estimated. To this aim, each spectrum was fitted after incrementing the energies $E_{L_i}^{\text{ef}}$ with its uncertainty (also displayed in Table III); these values ($\sim 5\%$) were quadratically added to the other terms to obtain the final uncertainty assigned to $\sigma_{L_i}^x$.

C. Comparison

In order to perform a comparison with theoretical models predicting the primary ionization cross section σ_{L_i} [33,34], a set fluorescence yields ω_{L_i} and Coster-Kronig transition probabilities f_{ij} must be addressed, as detailed in Eqs. (6). To this aim, the values summarized in Table IV were taken from Perkins *et al.* [35] and Campbell [36]. The resulting x-ray-production cross sections are compared in Fig. 5. It can be seen that in the case of L_2 and L_3 , both thick target methods are in good agreement with the theoretical cross

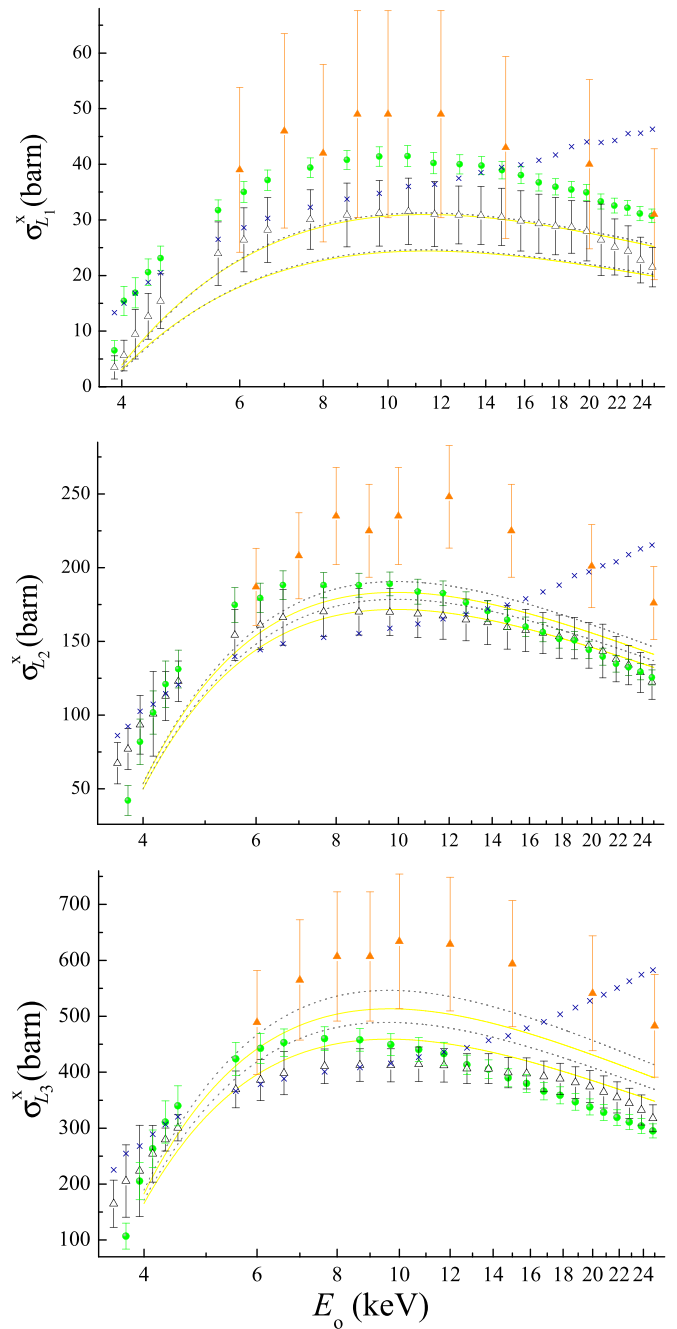


FIG. 5. L -subshell x-ray-production cross section for Ag. \bullet : Ionization distribution function approach; \times : original (uncorrected) integrodifferential method; \triangle : modified integrodifferential method; and \blacktriangle : previous thin target method [32]. Theoretical x-ray-production cross sections combined with the two sets of relaxation parameters (Table IV): — Bote *et al.* [33]; - - - Campos *et al.* [34].

sections. On the other hand, the results obtained for L_1 by the ionization distribution function method are deviated more than 25% from the theoretical models and from the modified integrodifferential method; this might be due to the high discrepancies in the Coster-Kronig transition probabilities f_{12} , since this parameter is involved only in the ionization distribution function method. The data previously obtained by using the thin sample method are clearly greater than all

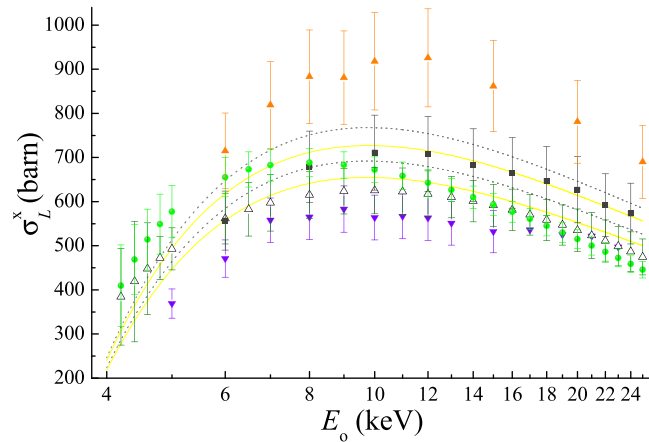


FIG. 6. Total L x-ray-production cross section for Ag. ●: Ionization distribution function; Δ : modified integrodifferential method; \blacktriangle : previous thin sample method [32]. \blacktriangledown : Wu *et al.* [12]; \blacksquare : Zhao *et al.* [37]. Theoretical x-ray-production cross sections combined with the two sets of relaxation parameters (Table IV): — Bote *et al.* [33]; - - - Campos *et al.* [34].

the other experimental and theoretical data, which may be attributed to systematic underestimates in the target thickness measurement. Finally, the results obtained with the original (uncorrected) integrodifferential approach appear to follow an unrealistic trend for high overvoltages.

With the purpose of comparing the present results with other authors, total L x-ray-production cross sections σ_L^x were also assessed. Since the cross sections measured for each E_o correspond to different effective energies $E_{L_i}^{ef}$ for each subshell (see Table III), the values $\sigma_{L_i}^x$ were fitted with functions analogous to Eq. (11) in order to assess them in E_o , the resulting values for $\sigma_L^x(E_o)$ being compared in Fig. 6. A very good agreement among all the data plotted is observed, except for those published by Wu *et al.* [12] and by Sepúlveda *et al.* [32]. The results obtained suggest that both thick target methodologies followed in this work provide consistent sets of values.

V. CONCLUSIONS

L -shell x-ray-production cross sections were determined in an Ag bulk target using a commercial wavelength-dispersive spectrometer. The modified integrodifferential method and the implementation of the ionization distribution function $\phi(\rho z)$ included in the POEMA software were used to this aim. The results found are equivalent between them and show a good agreement for most experimental and theoretical data reported in the literature. In the case of the total L x-ray-production cross section, both thick target methods considered allowed to determine data below 5 keV. Regarding L -subshell x-ray-production cross sections, the experimental data available were obtained by thin sample methods.

As expected, both thick target methods are clearly more useful for electron energies near the absorption edges, since the thin sample approximation requires target thicknesses too small, as well as long measurement times. The results obtained with the modified integrodifferential approach have been strongly modified for low and high electron energies when the corrections suggested here were included, following a trend apparently more realistic for the case of high overvoltages.

It is worth mentioning that the results obtained with the ionization depth-distribution function are quite straightforwardly assessed, producing a reliable set of data. In addition, as compared to the modified integrodifferential method, this approach bears smaller uncertainties, which may be especially helpful when managing weak signals, as is the case of low overvoltages.

ACKNOWLEDGMENTS

The authors would like to thank the Universidad Tecnológica Metropolitana (UTEM, Chile), CONICET and the Universidad Nacional de Córdoba (Argentina). They are also grateful to the Laboratorio de Microscopía y Análisis por Rayos X (LAMARX-UNC), where the experimental determinations were performed.

- [1] S. Khare, P. Sinha, and J. Wadehra, *Phys. Lett. A* **184**, 204 (1994).
- [2] P. Rez, *J. Res. Natl. Inst. Stand. Technol.* **107**, 487 (2002).
- [3] C. J. Fontes and H. L. Zhang, *Phys. Rev. A* **76**, 040703(R) (2007).
- [4] H. Tanaka, M. J. Brunger, L. Campbell, H. Kato, M. Hoshino, and A. R. P. Rau, *Rev. Mod. Phys.* **88**, 025004 (2016).
- [5] S. Segui, M. Dingfelder, and F. Salvat, *Phys. Rev. A* **67**, 062710 (2003).
- [6] D. Bote and F. Salvat, *Phys. Rev. A* **77**, 042701 (2008).
- [7] J. M. Fernández-Varea, S. Segui, and M. Dingfelder, *Phys. Rev. A* **83**, 022702 (2011).
- [8] X. Llovet, C. Powell, F. Salvat, and A. Jablonski, *J. Phys. Chem. Ref. Data* **43**, 013102 (2014).
- [9] Y. K. Kim and M. E. Rudd, *Phys. Rev. A* **50**, 3954 (1994).
- [10] P. Bernhardt and H. Paretzke, *Int. J. Mass Spectrom.* **223-224**, 599 (2003), in Memoriam of Werner Lindinger.
- [11] M. Guerra, P. Amaro, J. Machado, and J. P. Santos, *J. Phys. B: At., Mol. Opt. Phys.* **48**, 185202 (2015).
- [12] Y. Wu, Z. An, M. T. Liu, Y. M. Duan, C. H. Tang, and Z. M. Luo, *J. Phys. B: At. Mol. Opt. Phys.* **37**, 4527 (2004).
- [13] D. H. H. Hoffmann, C. Brendel, H. Genz, W. Löw, S. Müller, and A. Richter, *Z. Phys. A* **293**, 187 (1979).
- [14] H. Genz, C. Brendel, P. Eschwey, U. Kuhn, W. Löw, A. Richter, and P. Seserko, *Z. Phys. A* **305**, 9 (1982).
- [15] S. Reusch, H. Genz, W. Law, and A. Richter, *Z. Phys. D: At. Mol. Clusters* **3**, 379 (1986).
- [16] Z. An and Q. Hou, *Phys. Rev. A* **77**, 042702 (2008).
- [17] J. Zhu, Z. An, M. Liu, and L. Tian, *Phys. Rev. A* **79**, 052710 (2009).
- [18] R. Bonetto, G. Castellano, and J. Trincavelli, *X-Ray Spectrom.* **30**, 313 (2001).
- [19] S. P. Limandri, J. C. Trincavelli, R. D. Bonetto, and A. C. Carreras, *Phys. Rev. A* **78**, 022518 (2008).
- [20] A. Carreras, G. Castellano, S. Segui, and J. Trincavelli, *Phys. Rev. A* **102**, 012817 (2020).
- [21] P. D. Pérez, A. Sepúlveda, G. Castellano, and J. Trincavelli, *Phys. Rev. A* **92**, 062708 (2015).

- [22] S. P. Limandri, M. A. Z. Vasconcellos, R. Hinrichs, and J. C. Trincavelli, *Phys. Rev. A* **86**, 042701 (2012).
- [23] W. Bambynek, B. Crasemann, R. W. Fink, H. U. Freund, H. Mark, C. D. Swift, R. E. Price, and P. V. Rao, *Rev. Mod. Phys.* **44**, 716 (1972).
- [24] H. Paul and A. Schinner, *Nucl. Instrum. Methods Phys. Res., Sect. B* **227**, 461 (2005).
- [25] F. Salvat, J. M. Fernández-Varea, and J. Sempau, PENELOPE 2011: A code system for monte carlo simulation of electron and photon transport (OECD Nuclear Energy Agency, Issy les Moulineau, France, 2011).
- [26] R. Bonetto, A. Carreras, J. Trincavelli, and G. Castellano, *J. Phys. B: At. Mol. Opt. Phys.* **37**, 1477 (2004).
- [27] S. P. Limandri, A. C. Carreras, R. D. Bonetto, and J. C. Trincavelli, *Phys. Rev. A* **81**, 012504 (2010).
- [28] J. Riveros and G. Castellano, *X-Ray Spectrom.* **22**, 3 (1993).
- [29] T. Rodríguez, A. Sepúlveda, A. Carreras, G. Castellano, and J. Trincavelli, *J. Anal. At. Spectrom.* **31**, 780 (2016).
- [30] M. J. Berger, J. S. Coursey, M. A. Zucker and J. Chang, ESTAR, PSTAR, and ASTAR: Computer programs for calculating stopping-power and range tables for electrons, protons, and helium ions, version 1.2.3 (National Institute of Standards and Technology, Gaithersburg, MD, 2005), <http://physics.nist.gov/Star>.
- [31] D. E. Cullen, J. H. Hubbell, and L. Kissel, EPDL97: The Evaluated Photo Data Library '97 Version, Tech. Rep. No. UCRL-50400 6 (rev. 5) (Lawrence Livermore National Laboratory, Livermore, CA, 1997).
- [32] A. Sepúlveda, A. P. Bertol, M. A. Z. Vasconcellos, J. Trincavelli, R. Hinrichs, and G. Castellano, *J. Phys. B: At., Mol. Opt. Phys.* **47**, 215006 (2014).
- [33] D. Bote, F. Salvat, A. Jablonski, and C. Powell, *At. Data Nucl. Data Tables* **95**, 871 (2009).
- [34] C. Campos, M. A. Vasconcellos, J. Trincavelli, and S. Segui, *J. Phys. B: At. Mol. Opt. Phys.* **40**, 3835 (2007).
- [35] S. T. Perkins, D. E. Cullen, M. H. Chen, J. H. Hubbell, J. Rathkopf, and J. H. Scofield, Tech. Rep. No. UCRL-50400 30 (Lawrence Livermore National Laboratory, Livermore, CA, 1991).
- [36] J. L. Campbell, *At. Data Nucl. Data Tables* **85**, 291 (2003).
- [37] J. Zhao, Z. An, J. Zhu, W. Tan, and M. Liu, *Radiat. Phys. Chem.* **122**, 66 (2016).